Science and Technology of Advanced Materials

ISSN: (Print) (Online) Journal homepage: www.tandfonline.com/journals/tsta20

Macrophage targeting precision nanomedicine utilizing ROS-responsive metallozyme-loaded nanomicelle for enhanced treatment of gout-induced inflammation

Padmanaban Sathiyamoorthy, Shyam Vasvani, Sree Samanvitha Kuppa, Adityanarayan Mohapatra, Amal Babu, Yong-Yeon Jeong, Hong Yeol Yang, Jong Keun Seon, Chang-Moon Lee & In-Kyu Park

To cite this article: Padmanaban Sathiyamoorthy, Shyam Vasvani, Sree Samanvitha Kuppa, Adityanarayan Mohapatra, Amal Babu, Yong-Yeon Jeong, Hong Yeol Yang, Jong Keun Seon, Chang-Moon Lee & In-Kyu Park (22 Apr 2025): Macrophage targeting precision nanomedicine utilizing ROS-responsive metallozyme-loaded nanomicelle for enhanced treatment of gout-induced inflammation, Science and Technology of Advanced Materials, DOI: 10.1080/14686996.2025.2491304

To link to this article: https://doi.org/10.1080/14686996.2025.2491304

Publisher: Taylor & Francis & The Author(s). Published by National Institute for Materials Science in partnership with Taylor & Francis Group.
Journal: *Science and Technology of Advanced Materials*
DOI: 10.1080/14686996.2025.2491304

Macrophage Targeting Precision Nanomedicine Utilizing ROS-responsive Metallozyme-Loaded Nanomicelle for Enhanced Treatment of Gout-induced Inflammation

Padmanaban Sathiyamoorthy[a,#], Shyam Vasvani[a,b,#], Sree Samanvitha Kuppa[a,c,d,#], Adityanarayan Mohapatra[a,b], Amal Babu[a], Yong-Yeon Jeong[b,e,f], Hong Yeol Yang[c,d], Jong Keun Seon[a,c,d,*], Chang-Moon Lee[f,g,*], In-Kyu Park[a,b,*]

[a] Department of Biomedical Sciences and BioMedical Sciences Graduate Program (BMSGP), Chonnam National University Medical School, Hwasun 58128, Republic of Korea.

[b] DRCure Inc. Hwasun 58128, Republic of Korea.

[c] Department of Orthopaedics Surgery, Center for Joint Disease of Chonnam National University Hwasun Hospital, 322 Seoyang-ro, Hwasun-eup, Jeonnam 519-763, Korea.

[d] Korea Biomedical Materials and Devices Innovation Research Center of Chonnam National University Hospital, 42, Jebong-ro, Dong-gu, Gwangju 501-757, Korea.

[e] Department of Radiology, Chonnam National University Medical School and Hwasun Hospital, Hwasun, South Korea.

[f] Leading Research Center of Total Solution for Osteoporosis Treatment, Chonnam National University, Yeosu, 59626 Republic of Korea.

[g] School of Healthcare and Biomedical Engineering, Chonnam National University, Yeosu, Jeonnam, 59626, Republic of Korea.

 # Equal contributions

*** Corresponding authors**

Email: seonbell@chonnam.ac.kr *(J.K.S)*, cmlee@jnu.ac.kr *(C.M.L), and* pik96@jnu.ac.kr *(I.P)*

Abstract:

The excessive accumulation of monosodium urate crystals in joints leads to the pathological condition known as gout. While conventional treatments, which include Non-steroidal Anti-inflammatory Drugs, are available, their short half-life and low bioavailability limit their practical application. To overcome these limitations and leverage the Reactive Oxygen Species (ROS)-rich microenvironment, this study developed a novel ROS-responsive thioketal-linked hyaluronic acid-based micelle loaded with manganese oxide (HTO-MnO) for enhanced treatment. Following the synthesis of the HTO-MnO nanocomplex, the micelle was well characterized and the synthesized micelle were subjected to multiple tests to confirm their efficacy in reducing ROS. In addition, the *in-vitro* treatment of M1-polarized macrophages showed significant responses at both the gene and protein expression levels. Eventually, *in-vivo*

analysis of the HTO-MnO nanoparticles was performed in the MSU-induced arthritis mouse model. The elevated ROS levels in the ankle joint of the mice triggered the release of MnO nanoparticles from the HTO micelles, suppressing the ROS levels and repolarizing macrophages to their M0 state, thereby effectively mitigating inflammation. This study demonstrates the potential of nanocomplex to reduce ankle swelling and intrinsic ROS levels by targeting M1 macrophages. The results highlight its precise therapeutic mechanism to alleviate inflammation and treat gouty arthritis.

Keywords: Gout inflammation; Reactive Oxygen Species-responsive release; hyaluronic acid micelle

1. Introduction

Gouty arthritis is an inflammatory condition resulting from the accumulation of monosodium urate (MSU) crystals in the joints and surrounding tissues [1]. This medical condition occurs when blood uric acid levels exceed 6.8 mg/dL, referred to as hyperuricemia. As such, hyperuricemia is the root cause of gout and is characterized by repetitive attacks of acute arthritis due to the elevated formation of uric acid crystals in the blood, leading to inflammation and pain [2]. Among the symptoms of gout include frequent flares, inflammation, and intense pain, typically affecting the joints. The risk of gout attacks is higher following the consumption of foods containing dietary purines, which are metabolized into uric acid and can significantly increase uric acid levels in the blood [3].

In gout, interleukin-1β (IL-1β) plays a crucial factor in driving the inflammatory response and promoting the M1 pro-inflammatory phenotype in macrophages [4]. The activation of the NLRP3 inflammasome in macrophages by MSU crystals leads to the production of active IL-1β. This, in turn, promotes the M1 macrophage phenotype through the upregulation of inducible nitric oxide synthase (iNOS), tumor necrosis factor-alpha (TNF-α), IL-6, and other pro-inflammatory mediators [5]. Consequently, this process enhances the generation of Reactive Oxygen Species (ROS) and nitric oxide (NO), triggering a self-perpetuating cycle of inflammation and causing tissue damage.

Among the traditionally used gout treatments include Non-steroidal Anti-inflammatory Drugs (NSAIDs), corticosteroids, xanthine oxidase inhibitors, and uricosuric agents. Despite their effectiveness, these treatments often suffer from certain drawbacks, such as gastrointestinal toxicity, cardiovascular risks, nephrotoxicity, and frequent dosing requirements, as a result of their limited bioavailability and short half-life [6]. Alternatively, nanoparticle-based drug delivery systems offer a promising therapeutic approach with improved bioavailability, target-specific delivery to inflamed joints, sustained and controlled drug release, and minimal systemic adverse effects [7]. In particular, stimuli-responsive nanozymes have emerged as a potential treatment of gouty arthritis owing to their ability to target and release drugs specifically in the inflamed environment [8]. A wide range of nanozymes, including those based on carbon [9], cerium [10], iron [11], manganese [12], copper [13], and metal-organic framework [14], are currently being utilized to treat inflammation.

Considering the potential toxicity of metal-based nanoparticles when administered alone, research has revealed that encapsulating them within nanocarriers, such as micelles or liposomes, significantly enhances their biocompatibility [15]. For instance, Choi et al. encapsulated ROS-sensitive micelles with dMn_3O_4 nanoparticles to treat acute kidney injury. These nanoparticles, which exhibited strong catalase activity, were released specifically at inflammation sites to scavenge excess ROS, effectively reducing inflammation [16]. Similarly, Zhou et al. loaded ROS-responsive micelles with nanoceria and the therapeutic drug rhein for treating rheumatoid arthritis. The released nanoceria mitigated cellular oxidative stress through SOD-like activity, while rhein facilitated the polarization of macrophages from the M1 to the M2 phenotype, demonstrating effects on bone repair [17].

In this study, a novel ROS-responsive micelle consisting of hyaluronic acid (HA), a thioketal (TK) linker, and octadecylamine (O) was designed to carry metallic nanoparticle and release their therapeutic payload specifically in response to elevated ROS levels in inflamed joints. This unique integration of components and stimuli-responsiveness, which was termed HA-TK-O (HTO), has been applied to treat arthritis for the first time. The materials utilized for preparing the nano

micelles were selected after taking into account several key factors, including the outstanding biocompatibility of HA, its exceptional ability to target CD44 receptors overexpressed in

inflamed tissues, and its highly hydrophilic properties that improve circulation time and stability [18]. Specifically, a 35 kDa HA was applied in this study, given its ability to easily permeate filters with 220 nm pores, ensuring excellent tissue penetration—an essential feature for drug delivery applications [19]. In addition, the rapid degradation of TK linkers in high ROS environments enables site-specific release of encapsulated contents [20]. Meanwhile, O provides a hydrophobic core for the nanomicelle to encapsulate the hydrophobic MnO [21], which possesses an excellent catalase-like activity that efficiently scavenges ROS and generates oxygen, alleviating hypoxia [22].

2. Materials and Methods

Materials

The materials utilized in this study were procured through the following suppliers: medical-grade hyaluronic acid (HA) with an approximate molecular weight of 38 kDa (Bloomage Biotechnology Corp. Ltd., Jinan, China); octadecylamine (OA), N-hydroxysuccinimide (NHS), 3-mercaptopropionic acid, ethylenediamine (EDA), and 1-ethyl-3-(3-dimethylaminopropyl) carbodiimide (EDC) (Sigma-Aldrich, St Louis, MO, USA); 2,4,6-trinitrobenzene sulfonic acid (TNBSA or TNBS) (Thermo Scientific); N,N-dimethylformamide (DMF) (Merck, Darmstadt, Germany); uric acid (Alfa Aesar); 2',7'-dichlorodihydrofluorescein diacetate (DCFH-DA) kit (Abcam); tumor necrosis factor-alpha (TNF-α) and IL-6 enzyme-linked immunosorbent assay (ELISA) kits (Invitrogen).

Synthesis of Thioketal Linker (TK)

TK was synthesized using the established protocol [23]. Briefly, 3-mercaptopropionic acid (49 mmol) was dissolved in anhydrous acetone (98 mmol) in a 1:2 ratio and was kept under stirring along with dry hydrochloric acid (HCl) for ~6 hours at room temperature (RT). The resulting solution was cooled in an ice-salt bath until the solution underwent complete crystallization, and the crystals were collected. Then, the crystals were purified and washed with n-hexane, followed by cold Distilled Water using filter paper. Finally, the crystals isolated from the filter paper were lyophilized to obtain the final powder TK.

Synthesis of NH_2-TK-Octadecylamine (NTO)

NH_2-TK-Octadecylamine (NTO) was synthesized using a Monowave 400 microwave reactor (Anton Paar). Initially, EDC, NHS, and O were mixed in a 2:2:1 molar ratio and dissolved in DMF along with 100 mg of TK, then heated at 100°C for 3 hours. Following this, EDC, NHS, and EDA in a 2:2:1 molar ratio were added, and the reaction was allowed to proceed for an additional 3 hours. The reaction mixture was then diluted ten-fold with distilled water, and the precipitate formed was dialyzed against distilled water using a dialysis membrane with a molecular weight cut-off of 12–14 kDa for 24 hours. Finally, the purified product was lyophilized to obtain NTO.

Synthesis of HA-TK-Octadecylamine (HTO)

HA-TK-Octadecylamine (HTO) was synthesized by conjugating NTO to HA through an EDC/NHS reaction involving the amino group of NTO and the carboxylic group of HA. Briefly, a mixture of EDC:NHS (1:1 molar ratio) and 100 mg of HA dissolved in warm formamide was reacted with NTO (0.264 mmol of amine units, as determined by the TNBS assay) dissolved in 5 mL DMF for 3 hours. The resulting sample was dialyzed against phosphate-buffered saline (PBS) (pH 7.4) for 24 hours, followed by dialysis in distilled water for an additional 48 hours, and then lyophilized.

Synthesis of Hydrophobic Manganese Oxide (MnO)

MnO was synthesized following a previously established protocol [16]. Initially, 4 mmol sodium hydroxide (NaOH) in distilled water was added dropwise to 2 mmol manganese chloride ($MnCl_2$) with continuous stirring. Subsequently, a half-molar equivalent of $MnCl_2$ (1 mmol) to 1-dodecanethiol, acting as a hydrophobic layer, was introduced into the mixture with constant stirring. The resulting precipitate was collected via centrifugation and washed multiple times with ethanol and water to obtain the hydrophobic MnO (Figures S4, S5, and S6).

Preparation of ROS-responsive HTO-MnO

The HTO-MnO micelles were synthesized utilizing the oil-in-water (O/W) emulsion method. A solution of MnO and HTO in a 1:10 ratio was prepared and dissolved in dimethyl sulfoxide (DMSO) before being added dropwise into 10 mL of DW under a continuous probe sonication. The resulting mixture was stirred consistently for 24 hours at ambient temperature. Subsequently, the solution was dialyzed using a membrane with a molecular weight cut-off of

10–12 kDa against distilled water. The dialyzed solution was lyophilized to obtain the final product.

Synthesis of Needle-like Monosodium Urate (MSU) Crystals

MSU crystals were synthesized via the alkali-titration method [24]. In brief, 4 g of uric acid was dissolved in 800 mL of distilled water at 60℃. Subsequently, the pH of the solution was adjusted to 8.9 using 0.5 M NaOH, and the temperature was maintained at 60℃ until the uric acid was completely dissolved. After obtaining a clear solution, the reaction was stopped by incubating the solution at 4℃ for 24 hours. Then, the white precipitate was decanted and dried at 100℃ for 6 hours. Finally, pure MSU crystals were obtained through a purification process at 180℃ before each use. Figure S12 depicts the synthesis process of the MSU crystals.

Characterization of HTO-MnO Nanoparticles

The hydrodynamic size of the synthesized MnO nanoparticles was determined using Dynamic Light Scattering (DLS) with a Zetasizer Nano Z instrument (Malvern Instruments, UK). In addition, the surface charge analysis was performed using both the Zetasizer Nano Z and a Nanoparticle Tracking Analyzer (NTA) (Zetaview, Particle Metrix, Germany). Afterward, a Field Emission Transmission Electron Microscope (FE-TEM) (JEM-2100F, Jeol USA Inc., USA) was employed to examine the morphology of the nanoparticles, both with and without hydrogen peroxide (H_2O_2) treatment. Further confirmation of the chemical structure for TK, NTO, and HTO was performed using Fourier-transform Infrared (FTIR) spectroscopy (Spectrum Two, PerkinElmer, USA) and Proton Nuclear Magnetic Resonance (^{1}H NMR) spectroscopy (Bruker, USA) with a magnetic field strength of 400 MHz. Additionally, the surface chemistry and elemental composition of the synthesized MnO nanoparticles were analyzed using X-ray Photoelectron Spectroscopy (XPS) and Energy-Dispersive X-ray Spectroscopy (EDS), respectively.

Critical Micelle Concentration (CMC)

The Critical Micelle Concentration (CMC) of the synthesized HTO micelles was assessed using pyrene fluorescent probe method. HTO micelle solutions with concentrations ranging from 1 mg/mL to 1×10^{-5} mg/mL were prepared, with pyrene added at a concentration of 6.0×10^{-7} M. The solutions were then sonicated for 30 minutes before being incubated overnight at RT to

achieve equilibrium solubilization of pyrene. Subsequently, the fluorescence spectra for each concentration were determined at an excitation wavelength of 336 nm and an emission range of 360–450 nm.

Inductively Coupled Plasma-Mass Spectrometry (ICP-MS) Analysis

The Mn content (%) was analyzed via an 820 ICP-MS instrument (Varian Bruker, Billerica, MA, USA). Prior to the analysis, the loaded micelles underwent acid digestion in aqua regia (HCl:HNO_3 at a 3:1 ratio) and were left undisturbed for 4–6 hours. The solution was then diluted in deionized water before proceeding with the metal analysis.

Peroxide Scavenging Study

The catalase-like activity of the synthesized HTO-MnO micelles was evaluated using a fluorescence-based assay with terephthalic acid (TA) as the probe. In this analysis, the HTO-MnO was added with 1 mM H_2O_2, followed by the addition of 0.5 mM TA dissolved in DMF. Then, the sample was vortexed to ensure thorough mixing. The sample was left for 45 minutes, and the fluorescence levels were measured at an excitation wavelength of 320 nm and an emission value of 425 nm. The catalase-like activity was further characterized by repeating the assay at various HTO-MnO concentrations.

Additionally, TA and Ru(ddp) were employed as fluorescent probes to measure H_2O_2 scavenging activity using a Spark 10-M multimode microplate reader (Tecan Trading AG, Switzerland). The assay is based on the reaction between TA and H_2O_2, which produces 2-hydroxyterephthalic acid. This product emits a distinct fluorescence emission peak at 425 nm. In the presence of an effective catalytic system, such as MnO, H_2O_2 is decomposed into water and oxygen, leading to a decrease in the fluorescence intensity. This reduction corresponds with the catalase-like activity of the nanoparticles, making it an effective indicator to quantitatively assess the ability of the HTO-MnO micelles to catalyze the breakdown of H_2O_2, similar to the natural function of catalase.

Oxygen Generation Study

Ru(ddp) was also utilized as an oxygen generation probe to further validate the decomposition of H_2O_2 into water and oxygen. The sample was first mixed with 1 mM H_2O_2, followed by the addition of 1 μM Ru(ddp) dissolved in DMF. After the sample was thoroughly mixed, the oxygen generation level was measured through the quenching of Ru(ddp) fluorescence in the presence of H_2O_2 and the catalytic activity of the nanoparticles at an excitation wavelength of 440 nm and an emission range of 530–730 nm. To corroborate the fluorescence-based analysis, the oxygen-generating activity of MnO was directly monitored using an RDO Optical Dissolved Sensor (Thermo Scientific, USA). This real-time, direct, and quantitative assessment of the oxygen production during the catalytic decomposition of H_2O_2 ensures a complimentary evaluation of the HTO-MnO micelles' ability to catalyze the H_2O_2 breakdown into water and oxygen, further confirming their catalase-like activity.

Cell Viability Test

The toxicity of the produced HTO, MnO, and HTO-MnO nanoparticles was assessed using RAW 264.7 cells. Prior to the cell viability test, the cells were seeded in 96-well plates at a concentration of 1×10^4 cells/well in 100 μL of Dulbecco's Modified Eagle Medium (DMEM) supplemented with 10% Fetal Bovine Serum (FBS) and 1% antibiotics. The cell culture was then incubated for 12 hours. Then, the mature cells were exposed to varying concentrations of HTO, MnO, and HTO-MnO supplemented in 100 μL of DMEM culture media over 24 hours of incubation. Subsequently, the cytotoxicity profiles were examined using the WST-1 assay.

Intracellular Uptake Analysis

An intracellular uptake investigation was performed using IR780 dye as a substitute for MnO in the nanomicelle. The RAW 264.7 cells were exposed to 100 μg/mL of MSU for 12 hours to induce the development of M1 phenotypic macrophages. The cells were pre-exposed to an excess of HA for 4 hours to determine CD44-mediated cell uptake facilitated by HA. After washing, the cells were exposed to IR780, HTO-IR780, and PTO-IR780 for 2 hours (the latter was used as a control to demonstrate cell absorption by HA). The nanoparticle uptake was quantified by seeding the cells in a 6-well chamber, treated with 4% paraformaldehyde, and analyzed using flow cytometry to observe the cellular internalization of the dye, where the fluorescence signal serves as an indirect measure.

Intracellular ROS Assay

The 2,7-dichlorofluorescein diacetate (DCFH-DA) was used to measure intracellular ROS generation. Primarily, RAW 264.7 cells were cultured in a 24-well plate and exposed to 100 μg/mL of MSU (the concentration was selected based on previous studies) [25]. After 12 hours, the cell cultures were treated with HTO, MnO, and HTO-MnO for 24 hours. Then, the cells were exposed to 15 μM DCFH-DA for 40 minutes. After rinsing the cells with the provided washing solution, the cells were observed under a fluorescence microscope. The DCFH-DA signal was quantified using a multi-plate reader at an emission wavelength of 530 nm.

Flow Cytometry

The flow cytometry analysis utilized CD11b (APC) and CD86 (PE-A) antibodies purchased from Biolegend to assess the M1 macrophage population. This method also assessed the repolarization of M1 macrophage back to its non-inflammatory M0 macrophage state. Initially, RAW 264.7 cells were cultured in 90 mm dishes and were induced with 100 μg/mL of MSU. After 12 hours, the cultures were further treated with HTO, MnO, and HTO-MnO and incubated for 24 hours. The cells were subsequently trypsinized and treated with the two antibodies for 45 minutes. Finally, the cells were stained with 2% paraformaldehyde and analyzed using flow cytometry. The collected data was analyzed using FlowJo software.

Nitric Oxide (NO) Assay

The NO assay was performed via the Griess reagent method, which quantifies nitrite levels, a metabolite of NO, within the cell culture medium. RAW 264.7 cells were cultured in DMEM supplemented with 10% FBS at a seeding density of 5×10^4 cells/well in 24-well plates. Subsequently, the cells were induced with 100 μg/mL of MSU for 12 hours. Following this pre-treatment period, the MSU-induced cells were treated separately with varying concentrations of HTO, MnO, and HTO-MnO nanoparticles for an additional 24-hour incubation period. After completing the treatment, 100 μL of the cell supernatant from each experimental group was combined with an equal volume of Griess reagent. After incubating for 30 minutes, the nitrite concentration was determined using a BioTek visible spectrophotometer (Agilent Technologies, USA) at 540 nm. A standard curve constructed using standard sodium nitrite ($NaNO_2$) was employed to calculate the NO levels within each treatment group.

Polymerase Chain Reaction (PCR) Amplification

RAW 264.7 cells were seeded in 6-well plates at a density of 1×10^5 cells/well. Upon completion of the treatment period, cellular RNA was extracted using RNAiso Plus (TaKaRa, Japan). After RNA extraction, the complementary DNA (cDNA) was synthesized using RT premix (AccuPower, Bioneer) following the manufacturer's protocol. Then, PCR amplification was performed using a PCR master mix (Accupower, Bioneer), with the synthesized cDNA serving as the template. The PCR conditions were set as follows: initial denaturation at 95°C for 5 minutes, followed by denaturation at 95°C for 1 minute, annealing at a temperature dictated by the specific primers utilized (Table 1) for 30 seconds, extension at 72°C for 1 minute, and a final extension at 72°C for 5 minutes, with subsequent storage at 4°C.

Western Blot

Following the treatment period, protein samples were extracted from the cell culture using RIPA lysis buffer supplemented with protease and phosphatase inhibitors. The protein fraction was then isolated through centrifugation at 12,000 rpm for 20 minutes at 4°C to isolate. For the extraction of cytoplasmic and nuclear proteins, the NE-PER nuclear and cytoplasmic extraction reagents were utilized according to the manufacturer's protocol. Subsequently, equal amounts of the extracted proteins were loaded onto Sodium Dodecyl Sulfate–Polyacrylamide Gel Electrophoresis (SDS-PAGE) gels for electrophoresis, after which they were transferred onto polyvinylidene fluoride (PVDF) membranes. The membranes were then incubated in 5% skim milk for 1 hour at RT to block non-specific binding sites. After blocking, the membranes were probed overnight at 4°C with primary antibodies targeting iNOS (Santa Cruz, TX, USA), IL-1β (Santa Cruz, TX, USA), p65 (Cell Signaling, USA), lamin B1 (Cell Signaling, USA), IκBα (Cell Signaling, USA), NLRP3 (Cell Signaling, USA) and β-actin (Santa Cruz, TX, USA). Following the primary antibody incubation, the membranes were exposed to the corresponding secondary antibodies, including ZyMax goat anti-mouse IgG (Thermo Fisher Scientific, Waltham, MA, USA) for iNOS and β-actin, as well as mouse anti-Armenian hamster (Santa Cruz, TX, USA) for IL-1β, for 2 hours at RT. Protein bands were then visualized using Immobilon Chemiluminescent substrate (Merck Millipore, USA).

Immunofluorescence and Confocal Imaging

The protein expression pattern was examined through immunofluorescence and confocal imaging. RAW 264.7 cells were seeded onto coverslips at a density of 5×10^4 cells/mL in 6-well plates. Following the exposure to MSU crystals and treatment with HTO, MnO, and HTO-MnO, the cell culture media were discarded, and the cells were washed with PBS before being fixed in 4% paraformaldehyde for 20 minutes according to established protocols [26]. After fixation, the cells were rinsed with PBS and permeabilized with 0.5% Triton X-100 for 15 minutes. Subsequently, the cells were incubated in a 5% Bovine Serum Albumin (BSA) solution for 1 hour to block non-specific binding sites. After washing with PBS, the cells were exposed to primary antibodies (diluted 1:500 for iNOS, IL-1β, and p65) for 1 hour. The cells were rewashed with PBS, followed by treatment with fluorescent-labeled secondary antibodies and nuclear staining using DAPI for 5 minutes. Once the coverslips were mounted onto the glass slides using a mounting medium, the immunofluorescence and confocal imaging were examined using a BioTek Lionheart FX Agilent fluorescence imaging system (Seoul, Korea) at 20× magnification and a ZEISS LSM 700 confocal fluorescence microscope at 40× magnification.

Gouty Arthritis Treatment

The animal experiments conducted in this study were reviewed and approved by the Chonnam National University Medical School Institutional Animal Care and Use Committee (IACUC; project no: CNU IACUC-H-2024-23). All *in-vivo* assessments complied with the relevant regulations. Six-month-old male C57BL/6 mice were acquired from Orient Laboratory, South Korea. The gouty arthritis model was induced by directly injecting 100 mg/kg of MSU crystals in 50 mL of PBS into the mice's ankle joints. After 12 hours, the HTO-MnO nanoparticles were administered, and the joint swelling was monitored using a Vernier caliper for 96 hours. Following 12 hours of treatment, the mice were intraperitoneally injected with 200 µL of L-012 luminol solution (100 mg/kg), and results were observed using the NightOWL II LB 983 IVIS system (Germany).

3. Results and Discussion

Preparation, Synthesis, and Characterization of HTO-MnO Micelles with Loaded Hydrophobic MnO

Figures 1A and S1 illustrate a series of chemical reactions employed in this study for the development of a unique nanomicelle called HTO that responds to ROS. The characteristics of

the HTO were examined through ^{1}H NMR spectroscopy, as shown in Figure 1B. The presence of distinct individual peaks of TK linkers and O polymers confirmed their integration in the HTO molecules. Figure S2 A shows the individual components of the micelles for comparing the chemical shifts in ^{1}H NMR of HTO, particularly at δ 1.23 ppm, which corresponds to the methylene groups ($CH_2CH_2CH_2$), and at δ 0.83 ppm, which denotes the terminal methyl groups (CH_3) of the C18 chain. Furthermore, the chemical shift at δ 1.58 ppm is assigned to the $-SC(CH_3)_2$ methyl groups in TK (Figure 1B). Additionally, the distinct peak at δ 1.95 ppm represents the acetamido moiety ($-NHCOCH_3$) in the N-acetyl-d-glucosamine residue of HA [27]. Typically, N–H protons of amide groups appear in the 5–9 ppm range, with some signals detected around 8 ppm depending on the specific environment. This is also shown in the conjugation of TK to HA and O. Apart from that, the strength of specific signals in the NMR spectrum was compared to quantify the extent of the long-chain O attachment. Based on the results, about 80% of the potential attachment sites were occupied by O. To validate the degradation of the thioketal (TK) linker, we performed NMR analysis to demonstrate the degradation of the TK linker in the presence of ROS and to quantify the resulting degradation products (Figure S2 B). To confirm MnO release, we conducted experiments to measure the release of MnO under controlled ROS conditions. We tracked changes in proton environments caused by TK cleavage, specifically observing the disappearance of thioketal methylene protons (δ ~ 1.5-2.0 ppm) due to bond scission and the appearance of acetone protons (δ ~ 2.1 ppm) as a cleavage byproduct.

Thermogravimetric analysis (TGA) of MnO, HTO, and HTO-MnO revealed distinct thermal decomposition profiles as shown in the Figure S3 A and B. MnO exhibited minimal weight loss, indicating high thermal stability. HTO showed a significant 40% weight loss between 200-400 °C, attributed to organic component decomposition. HTO-MnO displayed an intermediate profile, with a reduced weight loss in the same range compared to HTO, confirming successful MnO incorporation, and a high-temperature plateau similar to MnO, demonstrating the composite's thermal stability. The NTO and HA attachment to both ends of the TK molecule was further validated using FTIR analysis, which is akin to evaluating the chemical fingerprint of the HTO. Figure S3 C shows the presence of S–C bonds and C=O bonds, which are part of the amide structure. In contrast to the bare HA and NTO, a unique peak appeared in the HTO polymer, which indicates the C–H bonds. The CMC of HTO was calculated to be 10.03 μg/mL.

The optimal synthesis of HTO-MnO was evaluated using varying HTO-to-MnO mass ratios. Based on the preliminary characterization studies, a mass ratio of 10:1.2 mg (HTO: MnO) was selected for subsequent experiments as shown in Figure S7. As per ICP-MS analysis, the precise loading content of MnO within the nanomicelles was approximately 5.8%. In terms of the DLS analysis, the HTO exhibited an average hydrodynamic size and surface charge of 193 ± 12.3 nm and -23.47 mV, respectively, compared to 212 ± 31.3 nm and -22.76 mV for HTO-MnO, as shown in Figures 1C and 1E followed by Nanoparticle Tracking Analysis (NTA) showing increase particle/mL after loading MnO shows the stability of micelles as shown in Figure 1F and 1G which showed the particle distribution to be in accordance to the DLS data. The DLS graphs of both HTO and HTO-MnO are provided in Figure S8. Furthermore, the stability of the nanomicelle across three different mediums (water, PBS, and 10% FBS) for 5 days was relatively similar, with an insignificant change in size, as depicted in Figure 1D. The ROS-sensitive destabilization via the degradation of the TK linker of HTO-MnO was observed by DLS and FE-TEM analysis after treating the samples with 1 mM H2O2. The atomic percentage of Mn in MnO and the elemental composition and chemical bonding state of the MnO surface were analyzed using EDS and XPS, as presented in Figure S4 and S5.

ROS-Responsive Behavior of the HTO-MnO Nanocomplex and Catalytic H_2O_2 Decomposition Analysis

According to the schematic representation of the ROS-responsive behavior of HTO-MnO in Figure 2A, the ROS-responsive cleavage of the TK linker in an H_2O_2-rich environment leads to the release of the loaded MnO. The size of the HTO-MnO micelles expanded significantly which suggests the disintegration of the original nanomicelle structure and the subsequent formation of larger aggregates. This phenomenon indicates a responsive behavior of HTO-MnO to the presence of H_2O_2 (Figure S9). The TEM images of HTO alone and HTO-MnO in Figures 2B and 2C, respectively, also correspond to the DLS results in Figure 1C. Besides, Figures 2D and 2E depict the TEM images of HTO and HTO-MnO after exposure to 1 mM H_2O_2, demonstrating their ability to degrade in a ROS-rich environment induced by H_2O_2. These images also show the ROS-responsive role of the TK linker, which disintegrates in the ROS-rich microenvironment, thereby releasing the loaded MnO. Furthermore, Figures 2F and 2G present the elemental mapping of the metallic MnO within the HTO-MnO nanocomplex before and after

H_2O_2 treatment. In particular, Figure 2G shows that the disintegration of the TK linker leads to the release of MnO from the HTO. Loss of structural integrity without changes in hydrodynamic diameter, suggesting localized matrix degradation rather than core destruction and size increases from ~100 nm to >1000 nm after ROS exposure. The potential mechanism is that the cleavability of TK by ROS leads to the hydrophobic metal nanoparticle removal from the micelle core, resulting MnO release.

Meanwhile, the catalytic activity of HTO-MnO towards H_2O_2 decomposition was determined using TA as the fluorescent probe. As depicted in Figure 2H, the HTO-MnO nanoparticles emitted a substantially reduced fluorescence intensity compared to the unloaded HTO micelles when exposed to H_2O_2 over time. This observation confirms the catalase-like activity of the MnO nanoparticles within the hybrid nanostructure to catalyze the decomposition of H_2O_2 efficiently. In order to further prove the catalase enzymatic activity of HTO-MnO, a concentration-dependent Ru(ddp) assay was carried out. Based on the results in Figures S10A and S10B, the HTO-MnO recorded a drastic increase in oxygen levels, followed by a steady rise. The fluorescence intensity of Ru(ddp) also decreased with higher O_2 levels, suggesting the efficient production of O_2. In contrast, bare micelles (HTO) did not show any significant oxygen generation, confirming that only the MnO nanoparticles possess the capability to generate oxygen when reacting with H_2O_2(as shown in Figure 2I).

In-vitro Analysis of the Anti-oxidative Effects of HTO, MnO, and HTO-MnO Nanoparticles in MSU-activated Mouse Macrophage Cells

In-vitro tests were conducted to assess the antioxidative efficiency of the micelles against RAW 264.7 cells. The toxicity of the HTO-MnO nanocomplex and its components (HTO and MnO) was first evaluated to determine their optimal doses for further therapeutic studies. At 100 μg/mL, the HTO-MnO nanocomplex showed 81–83% toxicity to the cells (Figure 3A). However, the cytotoxicity significantly decreased to 45–47% at 50 μg/mL HTO-MnO. On the contrary, the HTO exhibited 67% viability at 150 μg/mL, while MnO recorded a less toxic effect at concentrations below 6.25 μg/mL (Figures S11A and S11B). Therefore, the final working concentrations were set at 50 μg/mL for HTO-MnO and HTO and 5 μg/mL for MnO. The final

concentration of HTO-MnO was checked for RBC lysis and was found to be safe until 300 μg/mL (Figure S17).

The efficiency of the HTO, MnO, and HTO-MnO to reduce NO in MSU-induced RAW cells was assessed using the nitrite quantification method, with the established working concentrations employed. Figure S13 shows the NO release at various concentrations of MnO, HTO, HTO-MnO, and only HA after 12 hours of treatment. An increase in NO release was observed when induced with 100 μg/mL of MSU in the PBS group, while the administered MnO, HTO, HTO-MnO, and HA significantly reduced NO production (Figure 3B). In view that NO can modulate ROS production by regulating specific enzymes, such as NADPH oxidases, the DCFH-DA test was used to quantify ROS levels. Initially, the RAW cells recorded a significant increase in ROS levels after 12 hours of being induced with 100 μg/mL of MSU. However, following a 24-hour treatment with the nanoparticles, the MnO treatment showed a marked decrease in the green fluorescence intensity, showcasing its catalase-mimicking ability to reduce H_2O_2. The HTO treatment also exhibited a reduction in H_2O_2 levels compared to the MSU-induced group, suggesting that the TK within the nanocarrier reacted with H_2O_2, thereby lowering its concentration. Additionally, the ability of HA to be upaken by the cell via CD44 receptors facilitates interaction with NO, leading to a decrease in NO levels. In the HTO-MnO treatment, the combined action of both MnO and HTO significantly reduced H_2O_2 levels.

The DCFH-DA results were subsequently assessed qualitatively through inverted microscopic imaging and quantitatively through fluorescent intensity analysis (Figures 3C and 3D). The IR780 fluorescent dye was loaded into the nanomicelle to help visualize the nanocomplex uptake into the cells and analyzed using flow cytometry after 4 hours of treatment (Figures 3E and F). Based on the results, cells without IR780 exhibited no fluorescence, while those loaded with IR780 showed intense fluorescence, which indicates significant cell uptake of the micelles. Furthermore, this study utilized PTO, a previously synthesized material [16], to demonstrate the advantage of using HA as an integral component nanomicelle. PTO showed lower cellular uptake compared to the HTO group, which had a higher cellular uptake due to its ability to target CD44 in M1 macrophages. The selective uptake was proven by blocking the CD44 receptors with a ten-fold increase of HA 4 hours before treatment with the HTO nanomicelle. Thus, the results demonstrate the potential of HTO to specifically target the CD44 receptor in M1 macrophages.

Following the confirmation of NO release and ROS reduction, the nanocomplex was analyzed using flow cytometry to assess macrophage polarization. While MSU-induced macrophages shifted from the M0 state to the pro-inflammatory M1 phenotype, treatment with the nanocomplex drastically reduced the number of M1 macrophages (Figures 3G and H). However, the M1 macrophages did not transend to the M2 phenotype but instead exhibited a significant reduction in their population, indicating a decrease in pro-inflammatory activity. This decline in the M1 state aligns with past research, suggesting that while high molecular weight HA can induce the cell conversion to the M2 phenotype, medium molecular weight HA can revert them to the reduction of M1 phenotype [28].

Effects of HTO, MnO, and HTO-MnO on the Gene and Protein Expressions of Inflammatory Mediators in MSU-induced Cells

The treatment effects of HTO, MnO, and HTO-MnO nanoparticles on *in-vitro* IL-1β levels of MSU-induced inflammation cells were assessed by PCR and Western blot techniques. At the gene expression level, the MSU-induced group recorded elevated mRNA expression of pro-inflammatory cytokines compared to the control group, as evident in both iNOS and IL-1β levels. In comparison, the mRNA expression of IL-1β in both the MnO and HTO-treated groups showed a moderate decrease. Remarkably, the combined effect of HTO-MnO synergistically reduced the expression of both iNOS and IL-1β (Figures 4A–4C). A similar trend was observed at the protein expression level, where the IL-1β and iNOS levels decreased, confirming the inflammation-regulatory potential of the HTO-MnO nanocomplex (Figures 4D–4F). The inhibition of iNOS and IL-1β by the HTO-MnO nanocomplex was further validated through confocal microscopy (Figure 4 G-J) and immunofluorescence analysis (Figures S14 and S15), which yielded consistent results with the observed protein expression patterns.

Effect of HTO, MnO, and HTO-MnO Nanoparticles on the NF-κB Pathway

The NF-κB pathway serves a vital function in regulating pro-inflammatory gene expressions. In view of this, the impact of HTO, MnO, and HTO-MnO treatment was assessed by quantifying the levels of two key proteins in this pathway: p65 and IκBα. Typically, MSU stimulation leads to IκBα degradation, allowing p65 to translocate to the nucleus and activate gene expression. According to the findings, the MSU-induced group recorded a decreased IκBα level, which indicates proteasomal degradation in the cytoplasm. In contrast, the IκBα levels

slightly increased in both MnO and HTO-treated groups, suggesting that HA prevented IκBα degradation (Figures 5A–5C). Moreover, the HTO-MnO-treated group recorded a marked increase in the IκBα levels.

To complement these findings, the p65 levels were measured through nuclear protein detection. As expected, the reduction in IκBα corresponded with an increased translocation of p65 into the nucleus, signifying elevated levels of p65 expression. However, treatment with MnO and HTO resulted in reduced p65 expression, with a more significant decrease in the HTO-MnO-treated group. This observation highlights the synergistic effect of the HTO-MnO nanocomplex in suppressing the p65 expression. Confocal microscopic images further confirmed the observed p65 nuclear translocation from the Western blot results. These complementary approaches provide strong evidence that HTO and MnO (individually and in combination) are capable of modulating the NF-κB pathway (Figure 5D and 5E). The modulation of NLRP3 inflammasome activation was further validated using the HTO-MnO micelle. In the final treatment group, a significant reduction in NLRP3 inflammasome activation was observed, indicating a substantial decline in the inflammatory response, as demonstrated in Figures S16 A and B.

***In-vivo* Analysis of the Anti-inflammatory Effects of HTO, MnO, and HTO-MnO Nanoparticles in MSU-induced Arthritis Mouse Model**

Gouty arthritis was induced by injecting 2 mg of MSU (in 50 μL of PBS) into the articular ankle joint of the mice. The excessively high concentration of the MSU forms an acute swelling and inflammation in the foot paw (right) within 12 hours of the injection. This time point was set as the initial inflammatory condition in both the *In-vivo* Imaging System (IVIS) (Figure 6A) and the foot paw swelling analysis (Figure 6B). In the case of IVIS imaging, the intrinsic levels of H_2O_2 were measured using L-012 luminol solution, which uses H_2O_2 as a substrate and emits bright luminescence. The luminescence intensity increases as the levels of H_2O_2 increase. As shown in Figure 6C, the control group, which was not induced with the MSU crystals, showed no luminescence.

In contrast, the other groups were induced with MSU crystals and treated with MnO, HTO, and HTO-MnO for 24 hours. Subsequently, the luminol solution was injected into the peritoneal cavity of the mice and allowed for the reaction with its substrate for 15–20 minutes. The PBS group (MSU-induced mice without nanoparticles treatment) emitted a strong

luminescence upon reacting with H_2O_2. However, a drastic reduction in luminescence was observed in the case of MnO, HTO, and HTO-MnO-treated groups, which indicates a significant decrease in H_2O_2 levels. This was due to the ability of the MnO nanoparticles to degrade the intrinsic H_2O_2 and convert them into water and oxygen as byproducts, thus lowering the ROS level in the ankles of the mice. The HTO group also exhibited a major reduction in luminescence, proving that the TK linker reacts with the H_2O_2 and reduces them over time *in-vivo*. Ultimately, the HTO-MnO treatment group showed a significant decrease in the H_2O_2 level due to the synergistic effect of both MnO and HTO, thereby proving their significantly effective combinatorial complex. The luminescence was also quantified and analyzed to give a clear representation of the experiment, as depicted in Figure 6D.

The same concentration of MSU was injected into the right paw of the mice to validate the ankle swelling reduction of the gouty mice before and after treatment with MnO, HTO, and HTO-MnO, as portrayed in Figure 6B. The left ankle paw was left untreated as a control and baseline to compare with the change in the right ankle paw. The difference in ankle swelling was measured using vernier calipers for 96 hours. When compared to the PBS group, ankle swelling was evidently reduced in the treatment groups (MnO, HTO, and HTO-MnO). A steady and significant reduction in ankle swelling was more notable in the HTO-MnO group, proving the hypothesis of sustained and on-demand release of the MnO nanoparticle to relax the ROS-induced swelling. The presence of HA in the HTO micelles also aided in reducing the swelling.

To further prove the concept of immune cell infiltrations, the H&E staining was performed to measure the population of the immune cell. The control had sparsely populated cells, which grew into a densely populated cell after the ankle joint was induced with MSU. Intriguingly, the cell infiltrations significantly dropped following the treatment with MnO, HTO, and HTO-MnO (Figure 7A). Confocal imaging was further employed to evaluate the immune activation in the MSU groups and the treatment effects using IHC for iNOS (Figure 7B), the M1 marker CD86 (Figure 7C), and the M2 macrophage marker CD206 (Figure 7D). Comparatively, the iNOS expression spiked up in the MSU-induced group and was gradually reduced after treatment, consistent with the *in-vitro* NO release experiment (Figure 3B and S13). Apart from being considered a vital regulator of the NO release, the iNOS is associated with the recruitment of the M1 macrophages to the inflamed site (Figures 7B and 7E). To confirm this event, the

slides were stained with CD86 antibodies to identify the M1 subtype population. The MSU-induced group showed an increased M1 population, which steadily reduced following the treatment with MnO, HTO, and HTO-MnO (Figures 7C and 7F), similar to the iNOS results.

Furthermore, the M2 macrophage subtype was examined using the CD206 antibody. The MSU-induced group exhibited a reduced M2 macrophage population. In contrast, the treatment groups showed a steady increase in the population (Figures 7D and 7G). This increase was attributed to the regulation of cytokines, as both TNF-α and IL-6 concentrations were significantly reduced in the *in-vitro* supernatant analysis of these cytokines (Figure S18). Finally, to ensure the biosafety of the materials and the concentrations used in the animal experiments, histological analysis of major organs was performed using the H&E staining procedure. The results confirmed that there was no damage to the major organs after the treatment (Figure S19).

4. Discussion

This study demonstrated that the HTO, MnO, and the HTO-MnO nanocomplex effectively alleviated gouty arthritis inflammation and reduced ROS levels in both *in-vitro* and *in-vivo* models. The nanocomplex was synthesized using the EDC/NHS pathway, which enabled targeted delivery in ROS-rich environments facilitated by the TK linker. The formation of the nanocomplex was confirmed through DLS and NTA, and its composition was verified using ^{1}H NMR and FTIR evaluation. Furthermore, the ROS-responsive behavior of the nanocomplex was observed and confirmed through TEM images with and without H_2O_2. Additionally, the catalase-like activity and oxygen-releasing ability of MnO were validated using TA studies and the Ru(Dpp) assay.

Following the confirmation of the synthesized HTO-MnO nanocomplex, the potential of MnO nanoparticles, HTO micelles, and HTO-MnO nanoparticles in reducing inflammation was evaluated in both *in-vitro* and *in-vivo* gouty arthritis mouse models. These nanoparticles targeted specific inflammatory markers, focusing mainly on the iNOS and IL-1β levels. Prior research has elucidated the role of MSU crystals in stimulating iNOS production, especially in macrophages, via distinct signaling pathways [29]. Upon exposure to the MSU crystals, macrophages initiate an inflammatory response, often mediated through specific receptors, such as Toll-like Receptor 4 (TLR4) [30]. Activation of TLR4 by MSU triggers a signaling cascade that leads to a

significant increase in iNOS expression, which in turn generates NO, a key stimulant in inflammation and various physiological processes [31, 32].

In the context of gout arthritis, NO generated by iNOS contributes significantly to sustaining the inflammatory response triggered by MSU crystals. Numerous studies have also emphasized the critical role of IL-1β in gouty arthritis pathogenesis induced by MSU. For instance, the pivotal mediator role of IL-1β in the inflammatory cascade initiated by MSU crystals was evidenced in IL-1β knockout mouse models, which exhibited reduced paw swelling and lower clinical scores [33]. In this regard, the present study investigated the gene and protein expressions of IL-1β and iNOS, as well as conducting a NO assay, to explore the potential therapeutic effects of HTO, MnO, and HTO-MnO nanoparticles in mitigating gout. Hypothetically, MnO nanoparticles possess inherent catalase-mimicking activity owing to their known ability to reduce inflammation. Metallic particles, including Mn-based and Mn_3O_4 nanoparticles, have shown efficacy in scavenging ROS and attenuating inflammation *in-vivo* [34].

Similarly, HTO has been recognized for its anti-inflammatory properties and effectiveness as a targeting moiety, enhancing cellular uptake. HA-containing nanoparticles utilize HA as a targeting ligand due to its natural affinity for the CD44 receptor. The biocompatibility and ability of HA to prevent opsonization make it ideal for extending the circulation time of systemically administered nanoparticles [35, 36]. Notably, the molecular weight of HA affects its biological activity, with optimal signaling observed within a specific size range [37]. Hence, the HTO nanoparticle employed in this study, with a molecular weight of 35 kDa, is well-suited to aid cellular uptake and reduce inflammation, potentially contributing to the observed reductions in IL-1β expression [38], as shown in Figure 4.

The reversion of M1 macrophages to the M0 phenotype can be explained based on existing research indicating that the molecular weight of HA influences macrophage behavior. As such, low molecular weight HA (5 kDa or less) maintains macrophages in the pro-inflammatory M1 state, while high molecular weight HA (up to 3000 kDa) facilitates the anti-inflammatory M2 phenotype. The medium-low molecular weight HA used in this study suggests that HA is only capable of reverting macrophages to the M0 resting state but not to the M2 phenotype, as illustrated in Figures 3G and 3H [28]. Furthermore, Mn_3O_4 nanoparticles have been shown to

inhibit iNOS. It is hypothesized that the combined effect of HTO and MnO enhances the anti-inflammatory activity of the HTO-MnO nanocomplex, potentially boosting its cellular uptake and intracellular action.

According to the findings, the synergistic properties of MnO, HTO, and their combined effect in HTO-MnO nanocomplex were evident in both *in-vitro* experiments—including the NO release assay, DCFH-DA analysis, gene and protein expression assays, and confocal microscopic imaging and in the animal model. This was confirmed by the reduction in H_2O_2 levels, as monitored through IVIS imaging, in addition to the IHC analysis recording decreased iNOS and CD86 levels and increased CD206 levels. Scheme 1 provides a schematic representation of the mechanism of action of the nanocomplex. Overall, these results validate the hypothesis of this study and highlight the therapeutic potential of MnO, HTO, and their combined HTO-MnO nanocomplex.

5. Conclusion

This study successfully developed a ROS-responsive HTO nanomicelle comprising HA, TK linker, and O, loaded with catalase-mimicking MnO nanoparticles. Upon exposure to rich ROS environments, such as H_2O_2 and superoxide radicals, the HTO nanomicelle degrades and releases the MnO nanoparticles, alleviating inflammation in both cell studies and mouse models. The cell studies demonstrated the significant effect of the nanomicelles in reducing intracellular ROS and repolarizing the M1 macrophage while also suppressing the secretion of pro-inflammatory cytokines, such as TNF-α and IL-6. The HTO, MnO, and HTO-MnO treatment resulted in a substantial decrease in both mRNA and protein levels of IL-1β and iNOS, which represent key regulators of inflammatory pathways. Following that, the quantification of the immune cell infiltration for iNOS, CD86 (M1 macrophage marker), and CD206 (M2 macrophage marker) revealed reduced pro-inflammatory immune responses in-vivo. In conclusion, the findings of this study support the hypothesis that the anti-inflammatory properties of MnO are enhanced by HTO, indicating a synergistic effect. These results underscore the promising therapeutic action of HTO, MnO, and HTO-MnO nanoparticles in managing the inflammatory response associated with MSU-induced arthritis.

Acknowledgments

Author contributions:

S.P- Conceptualization, Analysis, Methodology, Investigation, Writing original draft

S.V- Conceptualization, Analysis, Methodology, Investigation, Writing original draft

S.S.K- Conceptualization, Analysis, Methodology, Investigation, Writing original draft

A.N.M- Analysis, Methodology

A.B- Analysis, Methodology

Y.Y.J- Investigation, Supervision

H.Y.Y- Investigation, Supervision

C.M.L- Investigation, Supervision, Review

J.K.S- Investigation, Supervision, Review

I.P- Investigation, Supervision, Review and Editing, Resource and Funding acquisition

Funding: This research was supported by grants from the Basic Science Research Program through the National Research Foundation of Korea (NRF) funded by the Ministry of Science, ICT, & Future Planning (RS-2023-00217471, 2020R1A5A2031185, and NRF-2020M3A9G3080282). The authors are also grateful to the Center for Research Facilities at the Chonnam National University for their assistance in the FE-TEM and The Korea Basic Science Institute (KBSI), Gwangju Centre for NMR analysis.

Conflict of Interest

The authors declare no conflict of interest.

Data Availability Statement

The data are freely available upon request.

Received:

Revised:

Published online:

References:

[1]. Tao H, Mo Y, Liu W, Wang H. A review on gout: Looking back and looking ahead. International Immunopharmacology. 2023;117:109977. doi: https://doi.org/10.1016/j.intimp.2023.109977.

[2]. Wang W, Kou J, Zhang M, Wang T, Li W, Wang Y, et al. A metabonomic study to explore potential markers of asymptomatic hyperuricemia and acute gouty arthritis. Journal of Orthopaedic Surgery and Research. 2023;18(1):96. doi: 10.1186/s13018-023-03585-z.

[3]. Yen Y-F, Lai Y-J, Hsu L-F, Chen L-J, Ku P-W, Inan-Eroglu E. Association between vegetarian diet and gouty arthritis: A retrospective cohort study. Nutrition, Metabolism and Cardiovascular Diseases. 2023;33(10):1923-31. doi: https://doi.org/10.1016/j.numecd.2023.04.008.

[4]. Shin JI, Lee KH, Joo YH, Lee JM, Jeon J, Jung HJ, et al. Inflammasomes and autoimmune and rheumatic diseases: A comprehensive review. Journal of Autoimmunity. 2019;103:102299. doi: https://doi.org/10.1016/j.jaut.2019.06.010.

[5]. Huang J-H, Chiang B-L. Regulatory T cells induced by B cells suppress NLRP3 inflammasome activation and alleviate monosodium urate-induced gouty inflammation. iScience. 2021;24(2):102103. doi: https://doi.org/10.1016/j.isci.2021.102103.

[6]. Haraoui B, Khraishi M, Choquette D, Lisnevskaia L, Teo M, Kinch C, et al. Effectiveness and Safety of Tofacitinib in Canadian Patients With Rheumatoid Arthritis: Primary Results From a Prospective Observational Study. Arthritis Care Res (Hoboken). 2023;75(2):240-51. Epub 20221010. doi: 10.1002/acr.24966. PubMed PMID: 35678771; PubMed Central PMCID: PMC10091934.

[7]. Zhu R, Niu Y, Zhou W, Wang S, Mao J, Guo Y, et al. Effect of nanoparticles on gouty arthritis: a systematic review and meta-analysis. BMC Musculoskeletal Disorders. 2023;24(1):124. doi: 10.1186/s12891-023-06186-3.

[8]. Zhang M, Tong W. Stimuli-responsive nanozymes for biomedical applications. Biomaterials Science. 2023;11(17):5769-80. doi: 10.1039/D3BM00884C.

[9]. Geng H, Chen J, Tu K, Tuo H, Wu Q, Guo J, et al. Carbon dot nanozymes as free radicals scavengers for the management of hepatic ischemia-reperfusion injury by regulating the liver inflammatory network and inhibiting apoptosis. Journal of Nanobiotechnology. 2023;21(1):500. doi: 10.1186/s12951-023-02234-1.

[10]. Cao Y, Cheng K, Yang M, Deng Z, Ma Y, Yan X, et al. Orally administration of cerium oxide nanozyme for computed tomography imaging and anti-inflammatory/anti-fibrotic therapy of inflammatory bowel disease. Journal of Nanobiotechnology. 2023;21(1):21. doi: 10.1186/s12951-023-01770-0.

[11]. Yuan R, Li Y, Han S, Chen X, Chen J, He J, et al. Fe-Curcumin Nanozyme-Mediated Reactive Oxygen Species Scavenging and Anti-Inflammation for Acute Lung Injury. ACS Central Science. 2022;8(1):10-21. doi: 10.1021/acscentsci.1c00866.

[12]. Xiong Y, Zhang Y, Zhou C, Yu T. ROS scavenging Manganese-loaded mesoporous silica nanozymes for catalytic anti-inflammatory therapy. Advanced Powder Technology. 2023;34(1):103886. doi: https://doi.org/10.1016/j.apt.2022.103886.

[13]. Liu T, Xiao B, Xiang F, Tan J, Chen Z, Zhang X, et al. Ultrasmall copper-based nanoparticles for reactive oxygen species scavenging and alleviation of inflammation related diseases. Nature Communications. 2020;11(1):2788. doi: 10.1038/s41467-020-16544-7.

[14]. Yu B, Sun W, Lin J, Fan C, Wang C, Zhang Z, et al. Using Cu-Based Metal–Organic Framework as a Comprehensive and Powerful Antioxidant Nanozyme for Efficient Osteoarthritis Treatment. Advanced Science. 2024;11(13):2307798. doi: https://doi.org/10.1002/advs.202307798.

[15]. Li F, Qin Y, Lee J, Liao H, Wang N, Davis TP, et al. Stimuli-responsive nano-assemblies for remotely controlled drug delivery. Journal of Controlled Release. 2020;322:566-92. doi: https://doi.org/10.1016/j.jconrel.2020.03.051.

[16]. Choi HS, Mathew AP, Uthaman S, Vasukutty A, Kim IJ, Suh SH, et al. Inflammation-sensing catalase-mimicking nanozymes alleviate acute kidney injury via reversing local oxidative stress. Journal of Nanobiotechnology. 2022;20(1):205. doi: 10.1186/s12951-022-01410-z.
[17]. Zhou F, Li M, Chen M, Chen M, Chen X, Luo Z, et al. Redox Homeostasis Strategy for Inflammatory Macrophage Reprogramming in Rheumatoid Arthritis Based on Ceria Oxide Nanozyme-Complexed Biopolymeric Micelles. ACS Nano. 2023;17(5):4358-72. doi: 10.1021/acsnano.2c09127.
[18]. Hou X, Zhong D, Chen H, Gu Z, Gong Q, Ma X, et al. Recent advances in hyaluronic acid-based nanomedicines: Preparation and application in cancer therapy. Carbohydrate Polymers. 2022;292:119662. doi: https://doi.org/10.1016/j.carbpol.2022.119662.
[19]. Jia X, Shi M, Wang Q, Hui J, Shofaro JH, Erkhembayar R, et al. Anti-Inflammatory Effects of the 35kDa Hyaluronic Acid Fragment (B-HA/HA35). J Inflamm Res. 2023;16:209-24. Epub 20230113. doi: 10.2147/jir.S393495. PubMed PMID: 36686276; PubMed Central PMCID: PMC9846287.
[20]. Xu X, Saw PE, Tao W, Li Y, Ji X, Bhasin S, et al. ROS-Responsive Polyprodrug Nanoparticles for Triggered Drug Delivery and Effective Cancer Therapy. Advanced Materials. 2017;29(33):1700141. doi: https://doi.org/10.1002/adma.201700141.
[21]. Pei Q, Jiang B, Hao D, Xie Z. Self-assembled nanoformulations of paclitaxel for enhanced cancer theranostics. Acta Pharm Sin B. 2023;13(8):3252-76. Epub 20230305. doi: 10.1016/j.apsb.2023.02.021. PubMed PMID: 37655323; PubMed Central PMCID: PMC10465968.
[22]. Wu J, Li S, Wei H. Multifunctional nanozymes: enzyme-like catalytic activity combined with magnetism and surface plasmon resonance. Nanoscale Horizons. 2018;3(4):367-82. doi: 10.1039/C8NH00070K.
[23]. Yue C, Yang Y, Zhang C, Alfranca G, Cheng S, Ma L, et al. ROS-Responsive Mitochondria-Targeting Blended Nanoparticles: Chemo- and Photodynamic Synergistic Therapy for Lung Cancer with On-Demand Drug Release upon Irradiation with a Single Light Source. Theranostics. 2016;6(13):2352-66. doi: 10.7150/thno.15433.
[24]. Yan F, Zhang H, Yuan X, Wang X, Li M, Fan Y, et al. Comparison of the different monosodium urate crystals in the preparation process and pro-inflammation. Advances in Rheumatology. 2023;63(1):39. doi: 10.1186/s42358-023-00307-1.
[25]. Mohapatra A, Rajendrakumar SK, Chandrasekaran G, Revuri V, Sathiyamoorthy P, Lee Y-K, et al. Biomineralized Nanoscavenger Abrogates Proinflammatory Macrophage Polarization and Induces Neutrophil Clearance through Reverse Migration during Gouty Arthritis. ACS Applied Materials & Interfaces. 2023;15(3):3812-25. doi: 10.1021/acsami.2c19684.
[26]. Kuppa SS, Kang JY, Yang HY, Lee SC, Sankaranarayanan J, Kim HK, et al. Hyaluronic Acid Viscosupplement Modulates Inflammatory Mediators in Chondrocyte and Macrophage Coculture via MAPK and NF-κB Signaling Pathways. ACS Omega. 2024;9(19):21467-83. doi: 10.1021/acsomega.4c01911.
[27]. Uthaman S, Parvinroo S, Mathew AP, Jia X, Hernandez B, Proctor A, et al. Inhibiting the cGAS-STING Pathway in Ulcerative Colitis with Programmable Micelles. ACS Nano. 2024;18(19):12117-33. doi: 10.1021/acsnano.3c11257.
[28]. Rayahin JE, Buhrman JS, Zhang Y, Koh TJ, Gemeinhart RA. High and Low Molecular Weight Hyaluronic Acid Differentially Influence Macrophage Activation. ACS Biomaterials Science & Engineering. 2015;1(7):481-93. doi: 10.1021/acsbiomaterials.5b00181.
[29]. Zhong CS, Zeng B, Qiu JH, Xu LH, Zhong MY, Huang YT, et al. Gout-associated monosodium urate crystal-induced necrosis is independent of NLRP3 activity but can be suppressed by combined inhibitors for multiple signaling pathways. Acta Pharmacol Sin. 2022;43(5):1324-36. Epub 20210810. doi: 10.1038/s41401-021-00749-7. PubMed PMID: 34376811; PubMed Central PMCID: PMC9061757.
[30]. Rossato MF, Hoffmeister C, Trevisan G, Bezerra F, Cunha TM, Ferreira J, et al. Monosodium urate crystal interleukin-1β release is dependent on Toll-like receptor 4 and transient receptor potential V1

activation. Rheumatology (Oxford). 2020;59(1):233-42. doi: 10.1093/rheumatology/kez259. PubMed PMID: 31298290.
[31]. Guoying L, Li L, Siyue Y, Lei L, Guangliang C. Total Saponin of Dioscorea collettii Attenuates MSU Crystal-Induced Inflammation by Inhibiting the Activation of the TLR4/NF-κB Signaling Pathway. Evid Based Complement Alternat Med. 2021;2021:8728473. Epub 20211020. doi: 10.1155/2021/8728473. PubMed PMID: 34721647; PubMed Central PMCID: PMC8550844.
[32]. Wang Q, Lin B, Li Z, Su J, Feng Y. Cichoric Acid Ameliorates Monosodium Urate-Induced Inflammatory Response by Reducing NLRP3 Inflammasome Activation via Inhibition of NF-kB Signaling Pathway. Evid Based Complement Alternat Med. 2021;2021:8868527. Epub 20210106. doi: 10.1155/2021/8868527. PubMed PMID: 33505510; PubMed Central PMCID: PMC7808822.
[33]. Mariotte A, De Cauwer A, Po C, Abou-Faycal C, Pichot A, Paul N, et al. A mouse model of MSU-induced acute inflammation in vivo suggests imiquimod-dependent targeting of Il-1β as relevant therapy for gout patients. Theranostics. 2020;10(5):2158-71. Epub 20200112. doi: 10.7150/thno.40650. PubMed PMID: 32104502; PubMed Central PMCID: PMC7019178.
[34]. Tootoonchi MH, Hashempour M, Blackwelder PL, Fraker CA. Manganese oxide particles as cytoprotective, oxygen generating agents. Acta Biomater. 2017;59:327-37. Epub 20170705. doi: 10.1016/j.actbio.2017.07.006. PubMed PMID: 28688986.
[35]. Li C, Zhao Z, Luo Y, Ning T, Liu P, Chen Q, et al. Macrophage-Disguised Manganese Dioxide Nanoparticles for Neuroprotection by Reducing Oxidative Stress and Modulating Inflammatory Microenvironment in Acute Ischemic Stroke. Advanced Science. 2021;8(20):2101526. doi: https://doi.org/10.1002/advs.202101526.
[36]. Chiesa E, Greco A, Riva F, Dorati R, Conti B, Modena T, et al. CD44-Targeted Carriers: The Role of Molecular Weight of Hyaluronic Acid in the Uptake of Hyaluronic Acid-Based Nanoparticles. Pharmaceuticals (Basel). 2022;15(1). Epub 20220117. doi: 10.3390/ph15010103. PubMed PMID: 35056160; PubMed Central PMCID: PMC8781203.
[37]. Pandey MS, Baggenstoss BA, Washburn J, Harris EN, Weigel PH. The hyaluronan receptor for endocytosis (HARE) activates NF-κB-mediated gene expression in response to 40-400-kDa, but not smaller or larger, hyaluronans. J Biol Chem. 2013;288(20):14068-79. Epub 20130324. doi: 10.1074/jbc.M112.442889. PubMed PMID: 23530033; PubMed Central PMCID: PMC3656264.
[38]. Gao Y, Sun Y, Yang H, Qiu P, Cong Z, Zou Y, et al. A Low Molecular Weight Hyaluronic Acid Derivative Accelerates Excisional Wound Healing by Modulating Pro-Inflammation, Promoting Epithelialization and Neovascularization, and Remodeling Collagen. International Journal of Molecular Sciences. 2019;20(15):3722. PubMed PMID: doi:10.3390/ijms20153722.

No.	Primer name	Forward	Reverse	Tm (°C)	Base pair
1	Mouse IL-1β	CTACCTGTGTCTTTCCCGTG	CCAGCAGGTTATCATCATC	F =55.7 R = 47	118
2	Mouse iNOS	CTCTGGAATTCACAGCTCAT	ATGATGGTCACATTCTGCTT	F = 55.14 R = 55	527
3	Mouse GAPDH	ATCACTGCCACCCAGAAGAC	ATGAGGTCCACCACCCTGTT	F = 58.7 R = 59.8	443

Table 1: Specific conditions for the PCR amplification.

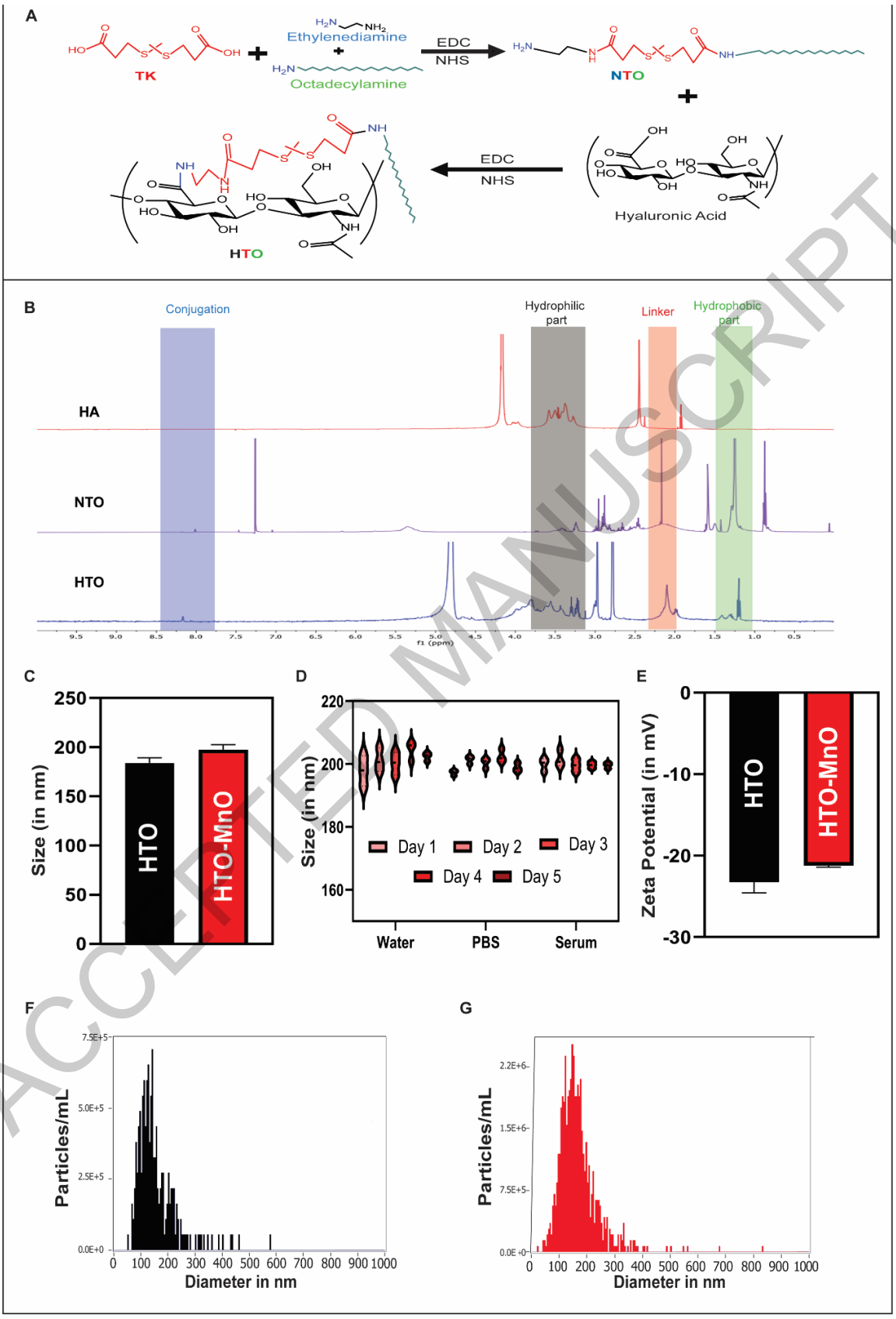

Figure 1: Nanoparticle synthesis and characterization. A) Schematic representation of the EDC/NHS reactions; B) ^{1}H NMR analysis of the synthesized nanomicelles showing the conjugation of HA with the ROS-responsive TK linker and O; C) Comparison of size distribution between HTO and HTO-MnO nanomicelles based on DLS; D) Surface charge analysis by zeta potential of HTO and HTO-MnO nanomicelles in water; and graphs depicting the size of E) HTO and F) HTO-MnO nanomicelles analyzed using NTA.

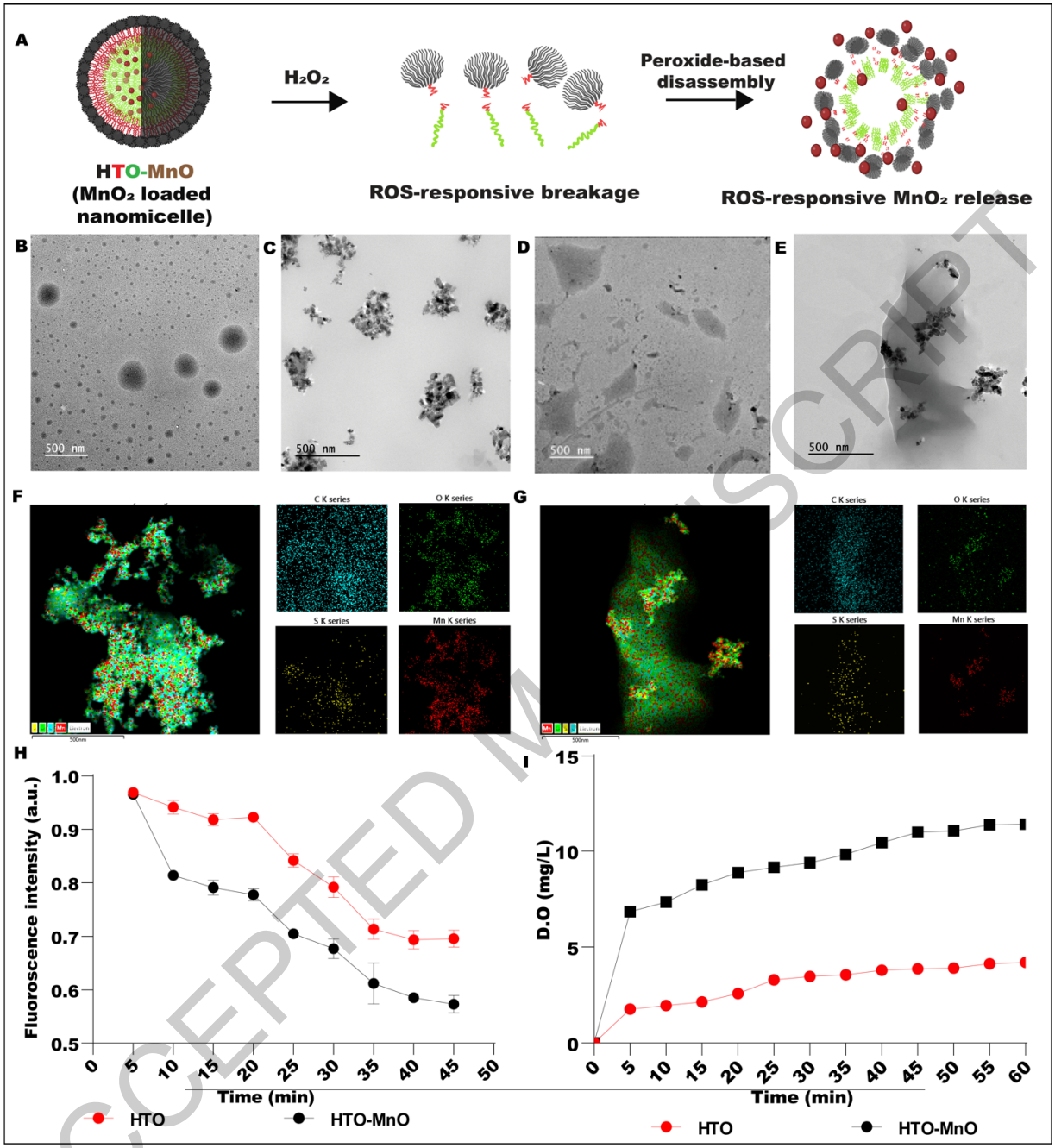

Figure 2: H_2O_2-responsive nanomicelle. A) Illustration of ROS-responsive breakage at the TK linker region; FE-TEM images of the B) HTO nanomicelle, C) HTO-MnO nanomicelle, D) HTO nanomicelle with 1 mM H_2O_2, and E) HTO-MnO nanomicelle with 1 mM H_2O_2; Elemental mapping of the F) HTO-MnO nanoparticle and G) HTO-MnO nanoparticle with the treatment of H_2O_2; H) TA assay showing the fluorescence reduction in HTO and HTO-MnO nanoparticles; and I) Oxygen generation ability of HTO and HTO-MnO nanoparticles with 1 mM H_2O_2.

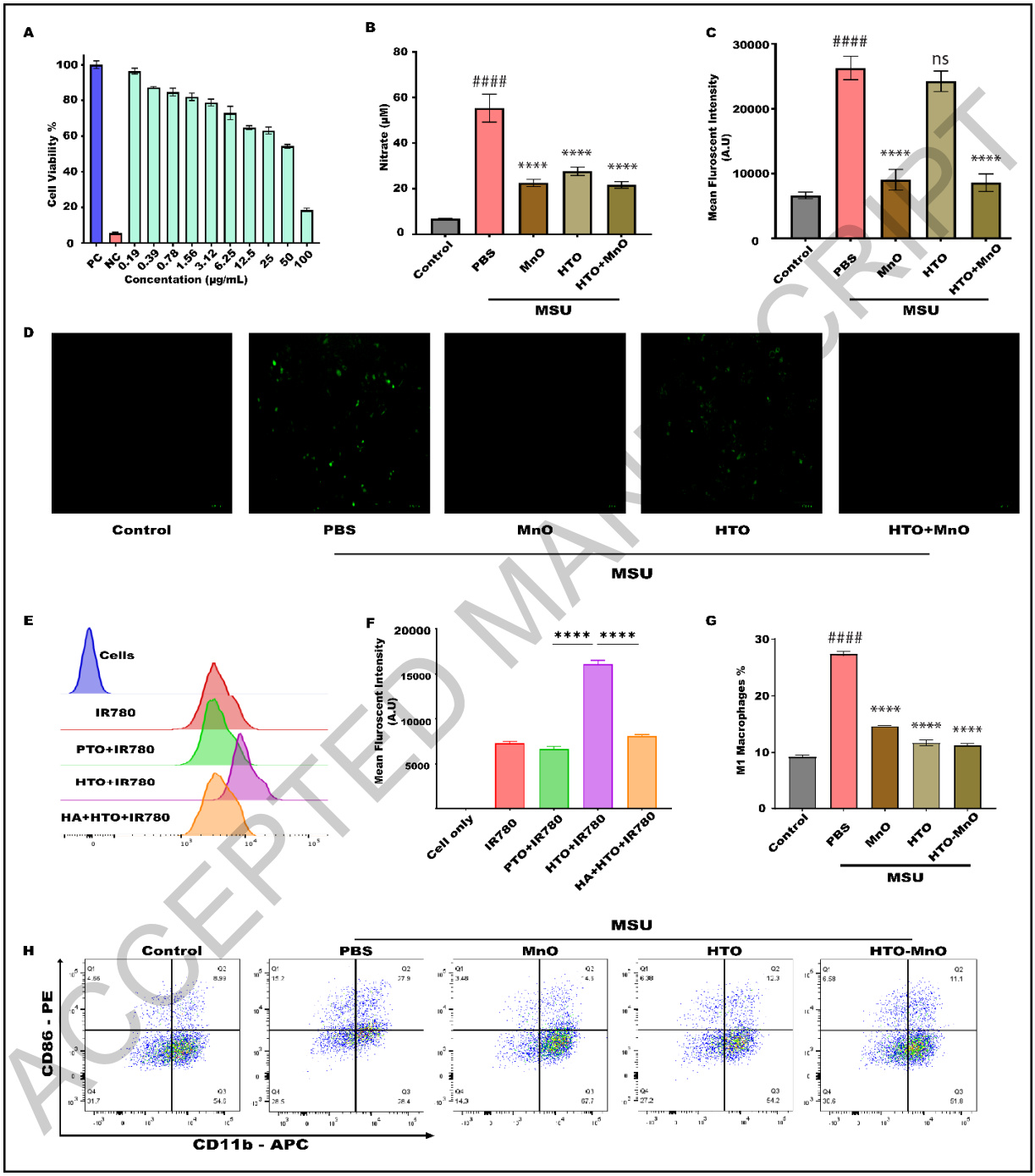

Figure 3: *In-vitro* analysis of the synthesized nanoparticles. A) WST-1 analysis demonstrating the cytotoxicity of HTO-MnO nanoparticles against RAW cells; B) NO release analysis using the Griess reagent; C) ROS regulation based on the quantitative DCFH-DA analysis; D) Inverted microscopic imaging of green fluorescence; E) Flow cytometry analysis of intracellular

nanoparticles uptake by M1 macrophages after 4 hours of the treatment; F) M1 macrophage repolarization analyzed using flow cytometry with CD11b and CD86 antibodies based on G) Quantitative analysis and H) Graphical representation. Statistical significance is indicated as follows: ## $p < 0.01$, ### $p < 0.001$, #### $p < 0.0001$ compared to the untreated control group of RAW cells; n.s. represents no significance; * $p < 0.05$, ** $p < 0.01$, *** $p < 0.001$, **** $p < 0.0001$ compared to the MSU-treated RAW cells.

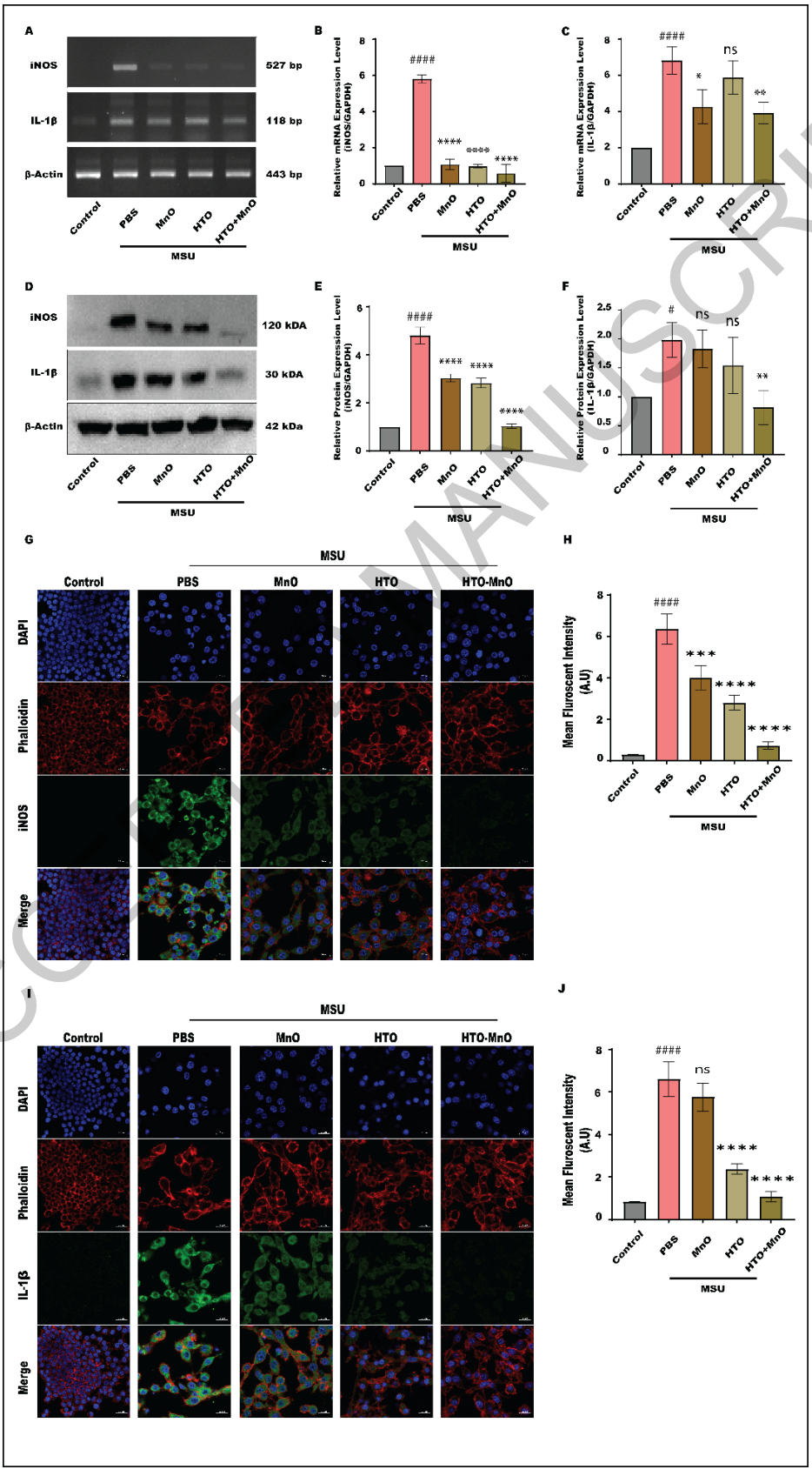

Figure 4: Treatment effect of HTO, MnO, and HTO-MnO nanoparticles on the gene and protein expressions in the MSU-induced group. A) Gene expression analysis using PCR; B) Relative mRNA expression levels of iNOS normalized to GAPDH; C) Relative mRNA expression levels of IL-1β normalized to GAPDH; D) Protein expression analysis using Western blot; E) Relative protein expression levels of iNOS normalized to β-actin; and F) Relative protein expression levels of IL-1β normalized to β-actin; Protein expression level analysis using confocal microscopic imaging. G) Confocal images of iNOS protein expression in M1 macrophages; H) Confocal images of IL-1β protein expression in M1 macrophages; I) Quantification of the iNOS-FITC signals; J) Quantification of the IL-1β -FITC signals. Statistical significance is indicated as follows: ## $p < 0.01$, ### $p < 0.001$, #### $p < 0.0001$ compared to the untreated control group of RAW cells; n.s. represents no significance; * $p < 0.05$, ** $p < 0.01$, *** $p < 0.001$, **** $p < 0.0001$ compared to the MSU-treated RAW cells.

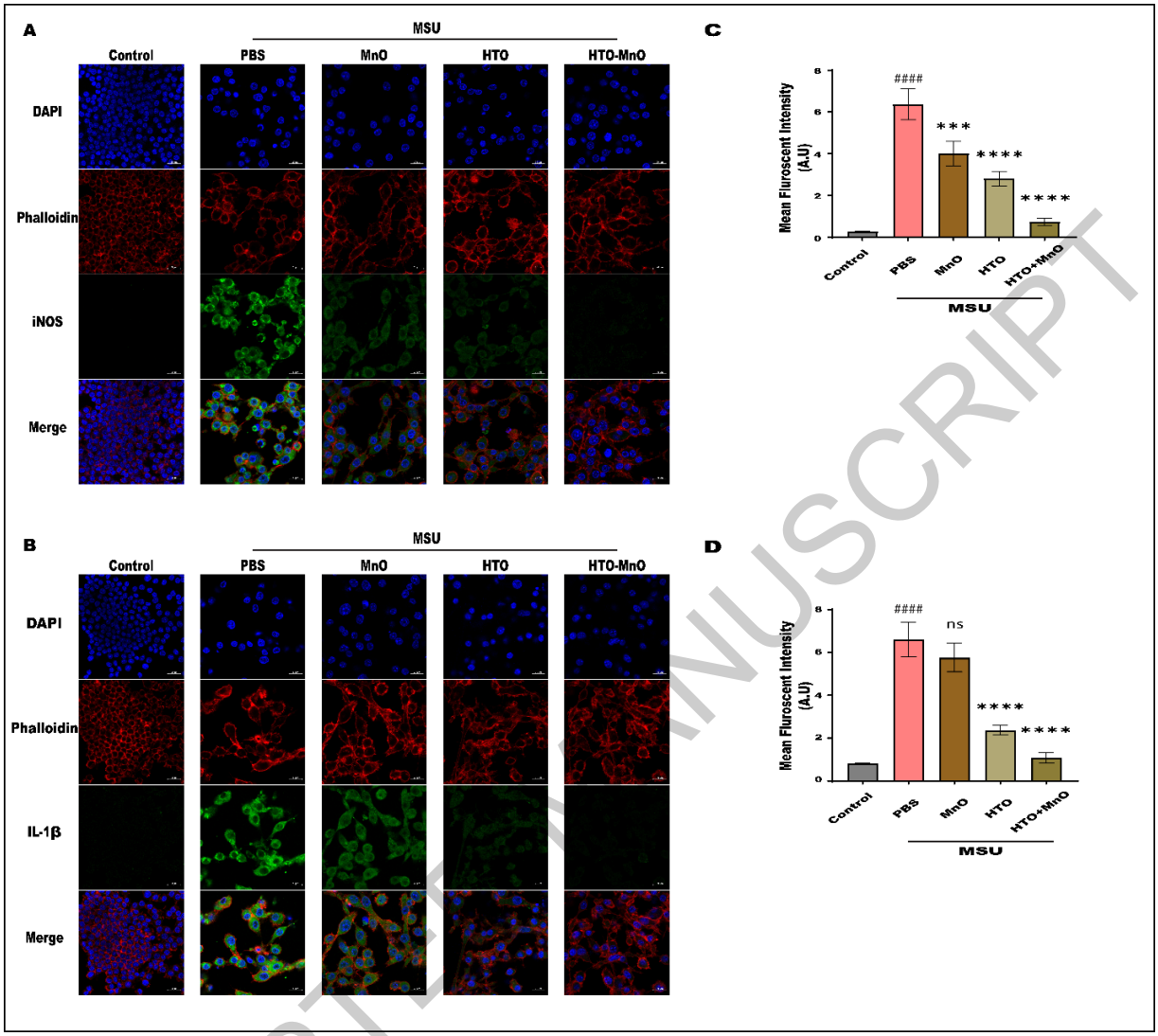

Figure 5: Treatment effect of HTO, MnO, and HTO-MnO nanoparticles on the protein expression in the MSU-induced group. A) Protein expression analysis using Western blot; B) Relative protein expression levels of nuclear p65 normalized to lamin B1; C) Relative protein expression levels of IκBα normalized to β-actin; D) Confocal microscopic images of p65 protein expression in M1 macrophages; and E) Quantification of p65-FITC signals. Statistical significance is indicated as follows: ## $p < 0.01$, ### $p < 0.001$, #### $p < 0.0001$ compared to the untreated control group of RAW cells; n.s. represents no significance; * $p < 0.05$, ** $p < 0.01$, *** $p < 0.001$, **** $p < 0.0001$ compared to the MSU-treated RAW cells.

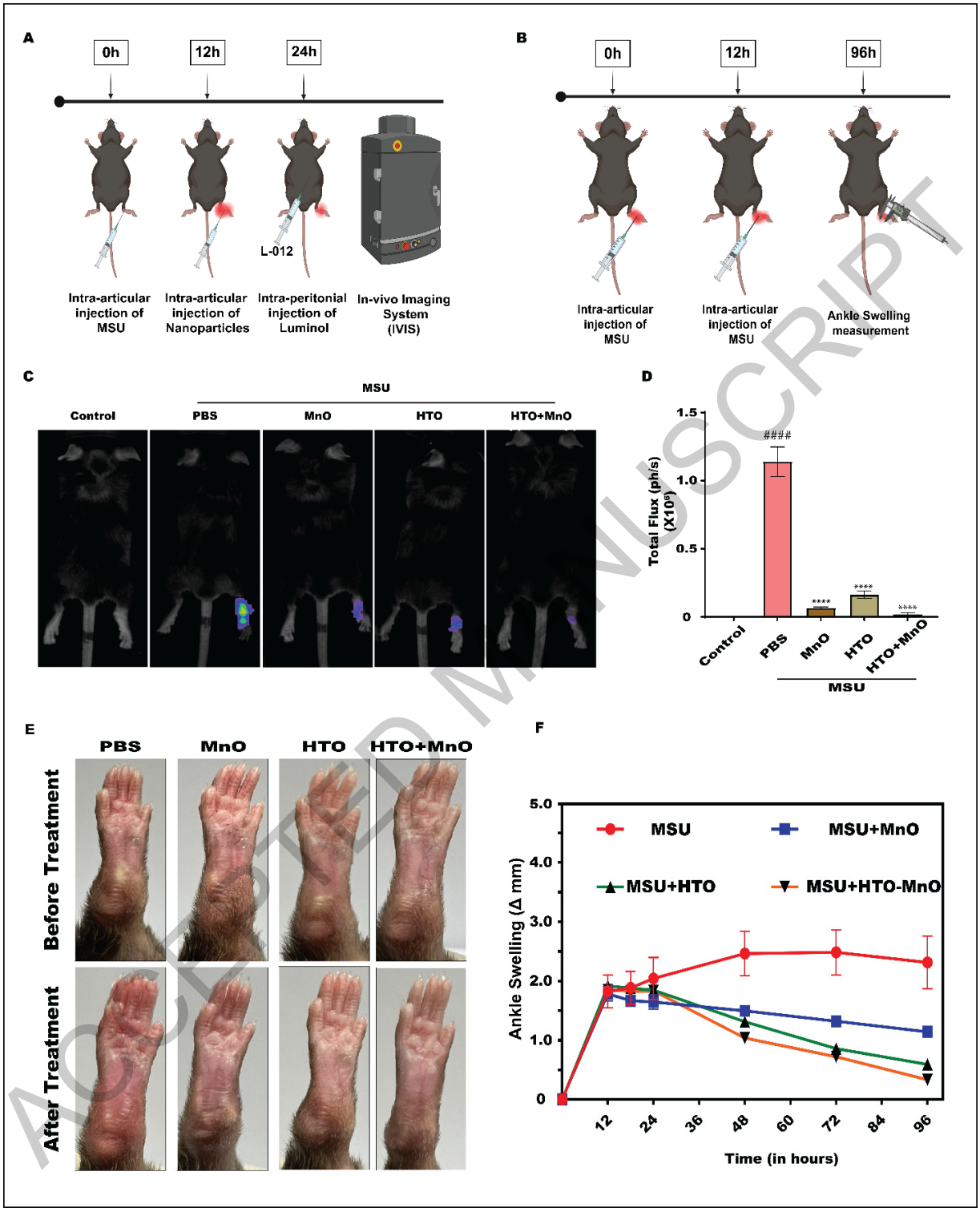

Figure 6: *In-vivo* experiments demonstrating the effects of nanoparticle treatment on the H_2O_2 levels and ankle swelling of MSU-induced mice. A) Schematic diagram of the IVIS experimental plan; B) Ankle swelling reduction experiment; C) IVIS results showing luminescent levels of intrinsic H_2O_2; D) Representative quantification graph; E) Images of mice foot paw before and

after the treatment; and F) Quantitative analysis of the difference in ankle swelling measured using vernier calipers. Statistical significance is indicated as follows: ## $p < 0.01$, ### $p < 0.001$, #### $p < 0.0001$ compared to the untreated control group of RAW cells; n.s. represents no significance; * $p < 0.05$, ** $p < 0.01$, *** $p < 0.001$, **** $p < 0.0001$ compared to the MSU-treated RAW cells.

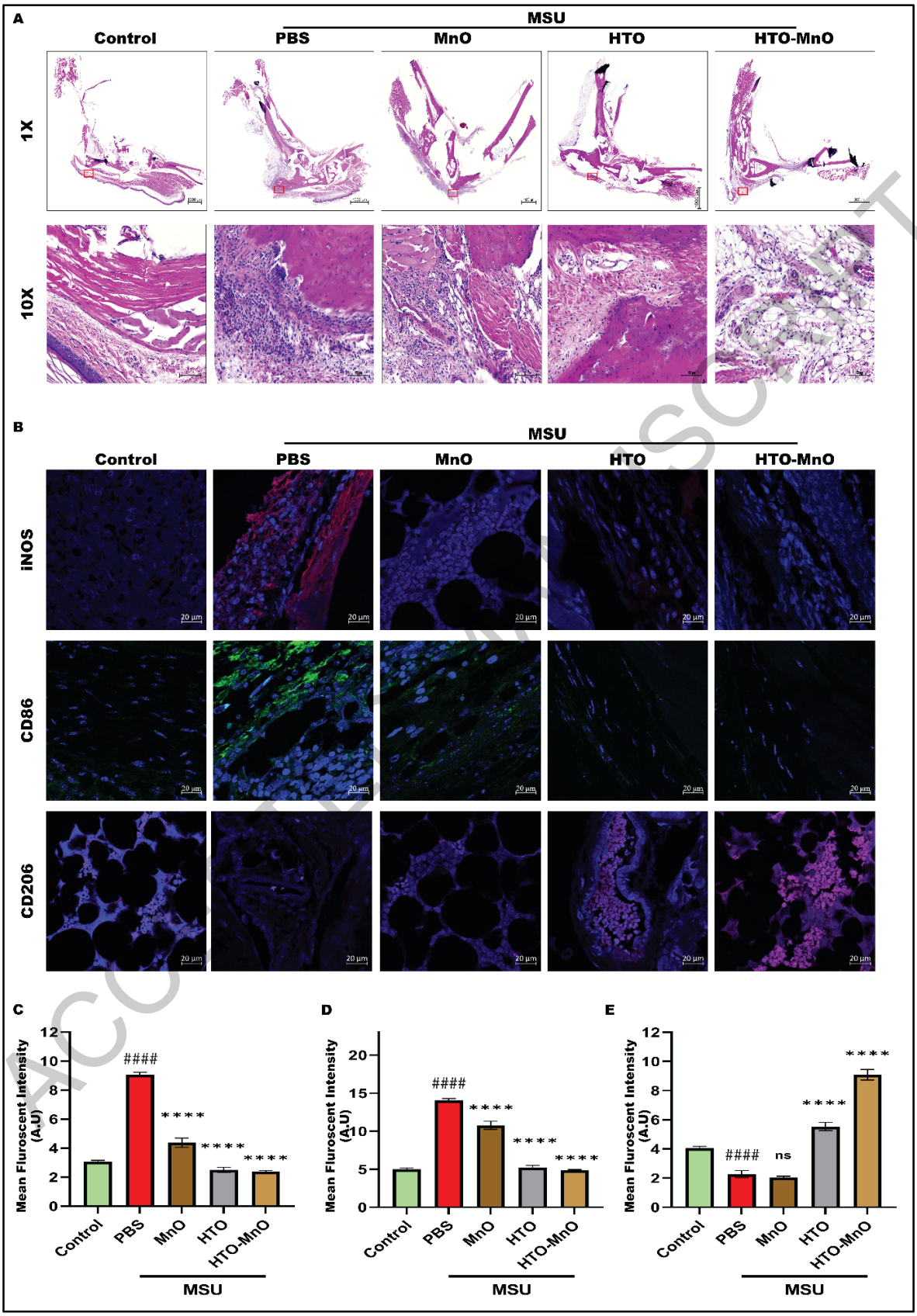
A
MSU
Control
PBS
MnO
HTO
HTO-MnO
1X
10X
B
MSU
Control
PBS
MnO
HTO
HTO-MnO
iNOS
CD86
CD206
20 µm
C
Mean Fluroscent Intensity (A.U)
12
10
8
6
4
2
0
####
****
****
****
Control
PBS
MnO
HTO
HTO-MnO
MSU
D
Mean Fluroscent Intensity (A.U)
20
15
10
5
0
####
****
****
****
Control
PBS
MnO
HTO
HTO-MnO
MSU
E
Mean Fluroscent Intensity (A.U)
12
10
8
6
4
2
0
####
ns
****
****
Control
PBS
MnO
HTO
HTO-MnO
MSU

Figure 7: Histological analysis to validate immune infiltration in the MSU-induced ankle joint of mice treated with HTO, MnO, and HTO-MnO nanoparticles. A) The H&E stained images of the cells (zoomed-in at 10× magnification); IHC stained images of the B) iNOS expression, M1 macrophages marked with CD86 receptors, and M2 macrophages marked with CD206 receptors; Quantification of expressions for C) iNOS, D) CD86, and E) CD206. Statistical significance is indicated as follows: ## $p < 0.01$, ### $p < 0.001$, #### $p < 0.0001$ compared to the untreated control group of RAW cells; n.s. represents no significance; * $p < 0.05$, ** $p < 0.01$, *** $p < 0.001$, **** $p < 0.0001$ compared to the MSU-treated RAW cells.

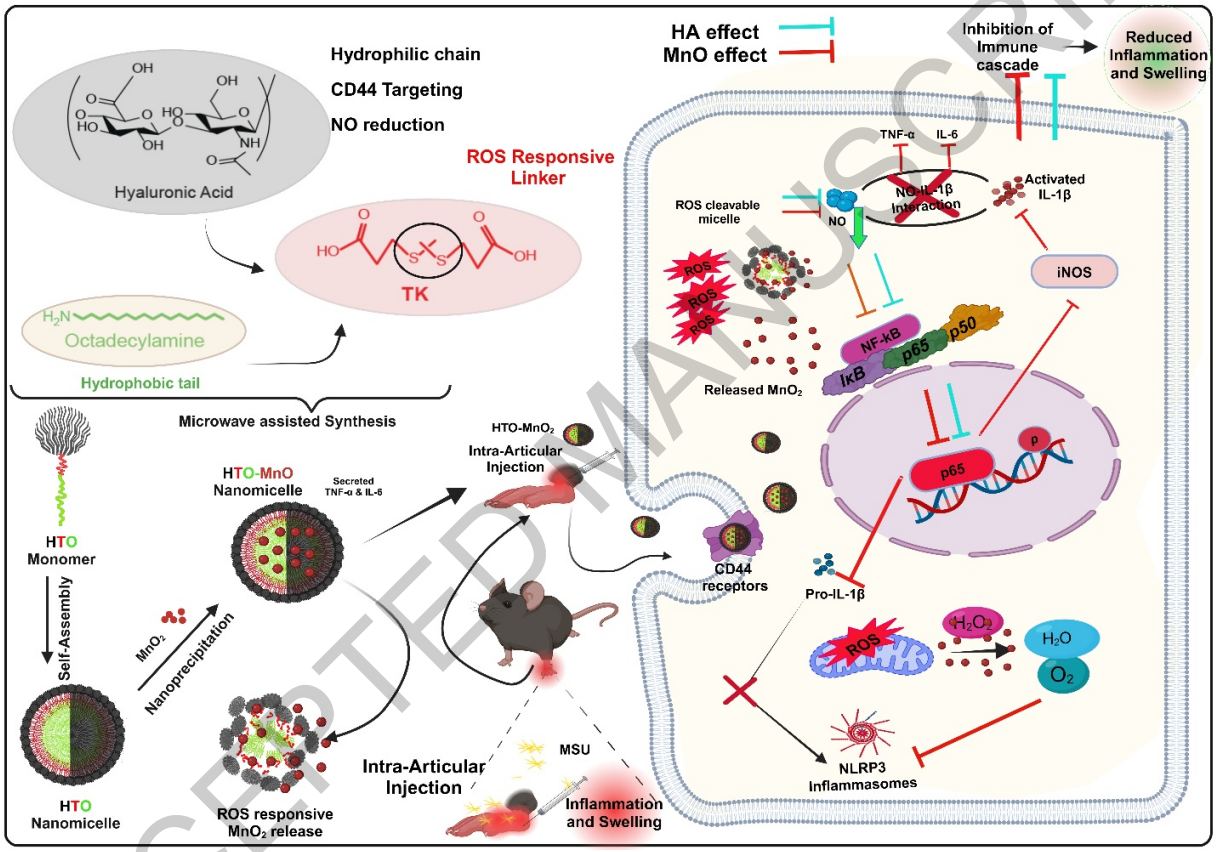

Scheme 1: Schematic representation of the HTO-MnO nanoparticle synthesis and its ROS-based release mechanism of MnO and alleviation of gouty arthritis severity following the treatment with HTO-MnO nanoparticles.

Employing manganese oxide-loaded ROS-responsive hyaluronic acid nanomicelle can be precise and serves as ROS scavenger and reduces inflammation. Combination of metallo-micelle is explored for first time in arthritis.